Response to Reviewer 2

"A global dataset of $\delta^{13}C\text{-}CH_4$ source signatures and associated uncertainties (1998–2022), with a sensitivity analysis to support isotopic inversions"

by Tapin et al. (essd-2025-668)

Submitted to Earth System Science Data (ESSD)

Legend:

Reviewer comments are reproduced in dark blue.

Author responses are in black.

Manuscript changes are shown in purple italics, with line numbers referring to the revised manuscript.

General response

We thank Reviewer 2 for the careful reading of the manuscript and for the constructive criticism. We are grateful that the reviewer recognises the timeliness and relevance of our work, the systematic uncertainty quantification, and the potential of the dataset to improve prior constraints in isotopic inversion systems. We have addressed all ten major comments through substantive revisions, including a new model–observation comparison section in the Supplement, an expanded critical assessment of inter-dataset systematic biases, additional sensitivity analyses on AGW sectoral granularity, an extended discussion of the OH-KIE parameterization and additional sinks (Cl, soil uptake), a new schematic diagram summarising the uncertainty propagation pathway, and a substantially revised discussion structure with improved readability and explicit regional case studies. We believe these revisions significantly strengthen the manuscript and address the concerns raised.

Response to major comments

M1. Absence of model–observation comparison

Reviewer comment: "The manuscript focuses on forward simulations and sensitivity analyses without comparison to atmospheric $\delta^{13}C\text{-}CH_4$ observations. While the authors justify this choice, the absence of validation limits confidence in the dataset and its applicability. Please include at least a first-order comparison with available surface or global $\delta^{13}C\text{–}CH_4$ observations to demonstrate the realism of the modeled fields."

Response: We agree that some form of observational reference would strengthen confidence in the dataset, even though we maintain our methodological position that the central deliverables of this paper are (i) a transparent and reproducible $\delta^{13}C\text{–}CH_4$ source signature dataset with quantified uncertainties, and (ii) a sensitivity analysis identifying the dominant uncertainty drivers. Full inversion-based validation, in which fluxes and signatures are jointly optimised, will be the subject of

a follow-up study because forward simulations alone cannot disentangle biases on fluxes from biases on signatures.

To address the reviewer's concern, we have added a new dedicated Section S4 "Model–observation comparison" in the Supplement, including two complementary first-order diagnostics:

(i) Globally averaged surface time series (1998–2022) of CH_4 mole fraction and $\delta^{13}C–CH_4$ for all forward sensitivity simulations, compared against the NOAA-INSTAAR globally averaged observations (Michel et al., 2024; Schuldt et al., 2025) with their ±1σ envelope (new Figure S11). This shows that most simulations remain within the observational envelope over the full period, while clearly identifying outliers (e.g., KIE_CANTRELL and ANTHROPO_GFEI) that are consistent with our sensitivity analysis findings.

(ii) Inter-hemispheric (NH–SH) gradient diagnostics for both CH_4 and $\delta^{13}C–CH_4$ averaged over 2016–2019 (new Figure S12). The inter-hemispheric gradient is a particularly stringent diagnostic because it isolates the joint contribution of source spatial distribution, transport, and oxidation chemistry while being insensitive to absolute calibration offsets and spin-up drift. The reference configuration reproduces the observed CH_4 gradient (~0.117 ppb) to within ~5%. For $\delta^{13}C–CH_4$, all simulations underestimate the observed gradient (−0.32‰ vs. −0.15 to −0.25‰ simulated), a residual bias which is fully consistent with our sensitivity analysis identifying OH-KIE and AGW source signatures as dominant drivers, and which reinforces our recommendations for inversion design.

We have also added a brief reference to this new comparison in the main text (Section 3.1.3) and in the Conclusions, while explicitly framing this as a plausibility reference rather than a formal validation, since forward simulations cannot rigorously validate the dataset without joint optimisation of fluxes and signatures.

Manuscript change (Section 3.1.3, L 298–299): *"See Sect. S4 in the Supplementary Material for the full 1998–2022 time series of all simulations compared to NOAA-INSTAAR observations (Michel et al., 2024; Schuldt et al., 2025)."*

Manuscript change (Conclusions, L 1082–1085): *"This study focused on developing and evaluating updated $\delta^{13}C$-CH_4 source signature maps through comparison with the literature, uncertainty quantification, and forward simulations. While direct validation using atmospheric data is beyond the scope of this paper, all necessary elements are provided, including gridded maps, uncertainty ranges, and sectoral breakdowns, to enable their integration into forward modeling and atmospheric inversions under optimal conditions."*

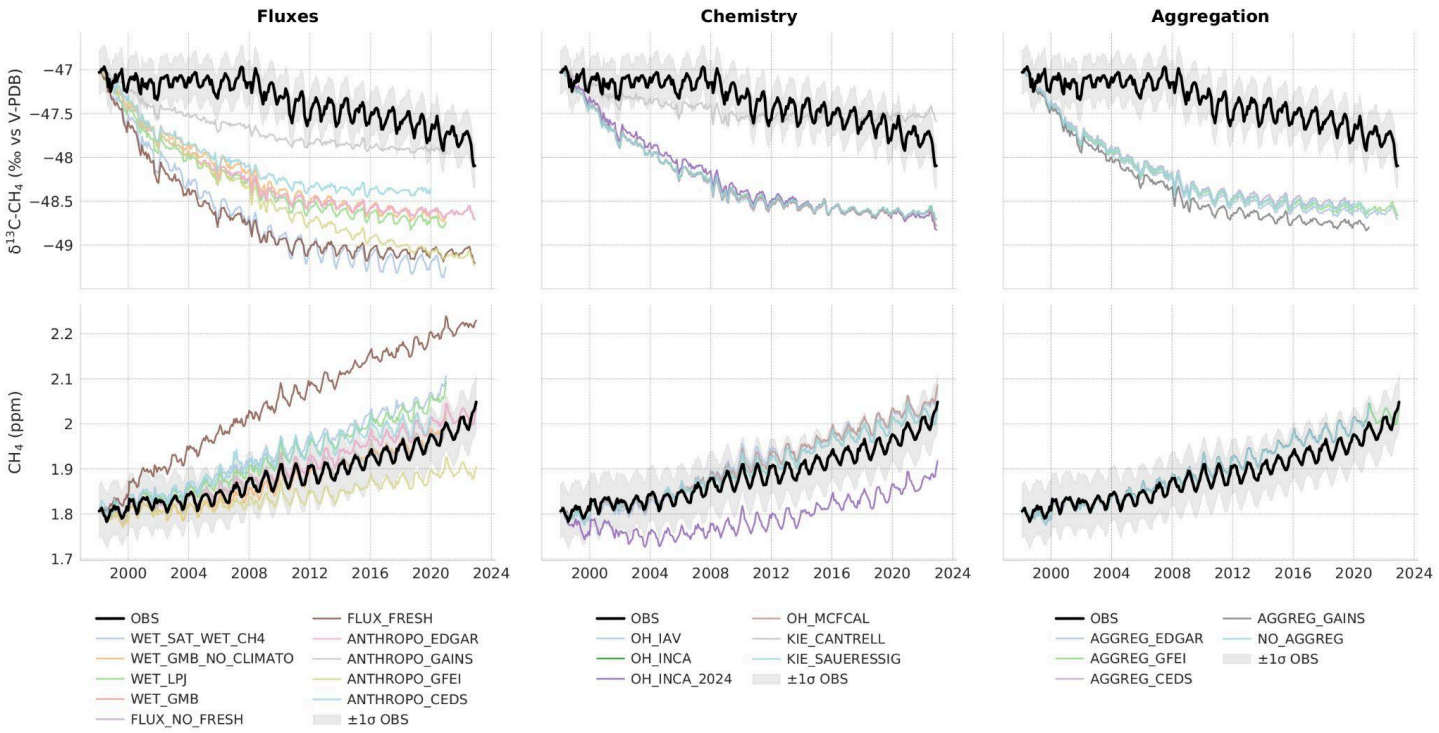

Figure S11. Globally averaged surface time series (1998–2022) of δ¹³C–CH₄ signal (top row, ‰ vs V-PDB) and CH_4 mole fraction (bottomrow, ppm) for all forward sensitivity simulations described in Table 3 of the main text, grouped by perturbation category: Fluxes (left), Chemistry (middle) and Aggregation (right). Black solid line: NOAA-INSTAAR globally averaged observations (Michel et al., 2024; Schuldt et al.,2025); grey shading:±1σobservational uncertainty. Coloured lines correspond to the individual simulations (see legends for configuration details). Simulations based on GAINS and GFEI inventories end in 2020 due to data availability.

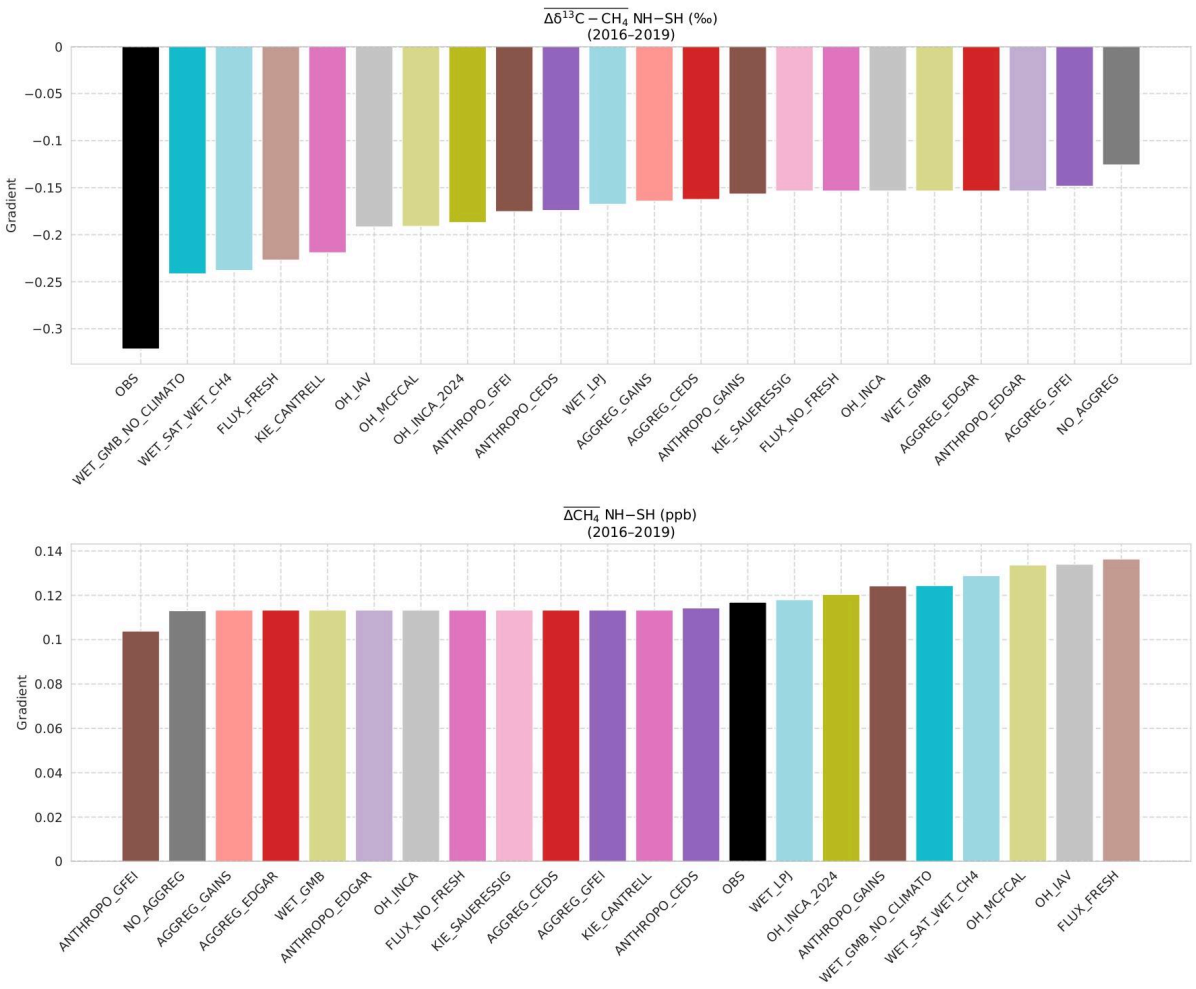

Figure S12. Inter-hemispheric gradient (NH–SH) of $\delta^{13}C$–CH_4 (top, ‰ vs V-PDB) and CH_4 (bottom, ppb) averaged over 2016–2019, for all forward sensitivity simulations described in Table 3 of the main text and for NOAA-INSTAAR observations (Michel et al., 2024; Schuldtet al., 2025) (black bar). Simulations are sorted by increasing gradient. The NH–SH gradient is computed from monthly surface fields, taking the difference between the latitudinally averaged Northern Hemisphere (0°–90°N) and Southern Hemisphere (90°S–0°) signals at the locations of NOAA-INSTAAR surface stations, and then averaged over 2016–2019.

M2. Inter-dataset inconsistencies and systematic bias propagation

Reviewer comment: "The isotopic source maps are largely derived from previously published datasets and literature synthesis. While this approach is necessary, the manuscript does not sufficiently address the potential propagation of systematic biases. Provide a more critical assessment of inter-dataset inconsistencies and discuss how these uncertainties may influence the final isotopic maps."

Response: We agree this point deserves a more critical treatment. We have substantially expanded Section 4.1.4 (Comparison with previous datasets) to include a new explicit discussion of three categories of systematic biases inherited from the underlying observational databases that are not captured by our quantitative σ_i:

(1) Uneven geographic coverage: the Sherwood et al. (2017, 2021) compilation underlying Lan et al. (2021a) is dominated by North American data; EMID (Menoud et al., 2024) improves European coverage but Africa, South America, and large parts of Asia remain under-sampled. Tropical wetlands are represented through fewer campaigns than boreal/temperate ones, and recent tropical measurement programs (France et al., 2022; Nisbet et al., 2021; Shaw et al., 2022) have not yet been integrated into process-based wetland isotope models.

(2) Methodological heterogeneity: literature signatures are typically arithmetic means while our sector values are flux-weighted; we explicitly quantify how this difference propagates for individual sub-sectors (e.g., the ~7‰ difference for coal between our flux-weighted estimate and the Menoud et al. (2022) arithmetic mean is shown to result from emphasis on high-emitting regions like China and India). For agricultural waste specifically, the inter-dataset spread (−52 to −57.8‰) exceeds the sub-sector uncertainty σ_i, pointing to genuine methodological heterogeneity in the definition of this sub-sector.

(3) Limited temporal representativeness: signatures are held constant for most sub-sectors over 1998–2022, while documented trends linked to evolving livestock feed composition, atmospheric $\delta^{13}C–CO_2$ changes, or gas processing practices (Chang et al., 2019) are not explicitly represented.

We have also added an explicit discussion of how these biases propagate to the aggregated maps depending on the flux-weighting scheme: biases affecting small-flux sub-sectors (termites, oceans) have limited impact, while those affecting high-emitting sub-sectors (livestock, oil and gas, tropical wetlands) propagate more directly to the modeled atmospheric $\delta^{13}C–CH_4$ signal, consistent with the sensitivity hierarchy reported in Table 6.

Manuscript change (Section 4.1.4, L 644–661): *“*

Beyond these sub-sector-specific differences, the inter-dataset inconsistencies are of the same order as the sub-sector uncertainty σi and point to systematic biases inherited from the underlying observational databases, which σi does not capture. At the sub-sector level, σi reflects the statistical dispersion within the sampled measurements (Menoud et al., 2022), not the representativeness of that sample relative to the true global distribution of emission sources. We identify three main systematic biases:

– Uneven geographic coverage: the compilation from Sherwood et al. (2017, 2021) underlying Lan et al. (2021a) is dominated by North American data, EMID (Menoud et al., 2024) improves European coverage but Africa, South America, and large parts of Asia remain under-sampled; tropical wetlands are represented through fewer campaigns than boreal/temperate ones, and recent tropical measurement programs (France et al., 2022; Nisbet et al., 2021; Shaw et al., 2022) have not yet been integrated;

– Methodological heterogeneity: literature signatures are arithmetic means while our sector values are flux-weighted;

– Limited temporal representativeness: signatures are held constant for most sub-sectors over 1998–2022, while documented trends linked to evolving livestock feed composition or gas processing practices (Chang et al., 2019) are not explicitly represented.

The propagation of these biases to the aggregated maps depends on the flux-weighting scheme: biases affecting small-flux sub-sectors (termites, oceans) have limited impact, while those affecting high-emitting sub-sectors (livestock, oil & gas, tropical wetlands) propagate more directly to the modeled atmospheric δ13C-CH4 signal, consistent with the sensitivity hierarchy reported in Table 6."

M3. Finer disaggregation of the AGW sector

Reviewer comment: "The agriculture and waste sector is identified as the dominant source of uncertainty, yet it is treated in a relatively aggregated manner. Where possible, further disaggregate AGW into sub-categories (e.g., livestock, rice paddies, waste management), or include sensitivity analyses demonstrating the effect of finer sectoral partitioning."

Response: We agree that AGW deserves particular attention given its dominant role. We would like to clarify that AGW is in fact already disaggregated in our framework into five sub-sectors (livestock, rice, landfills, wastewater, agricultural waste), each with its own isotopic signature and flux distribution (Table 1). Both the aggregated five-sector maps and the underlying 14 sub-sector maps are publicly distributed (Code and data availability section), so users can re-aggregate according to their own classification.

We have addressed the reviewer's concern through three substantive additions:

(1) Explicit AGW sub-sector breakdown in Section 4.2.1: we now state that livestock and rice together account for ~62% of AGW emissions and carry the most depleted signatures (−65.8‰ and −59.9‰), while waste-related sub-sectors (−50.9 to −56.2‰) make up the remaining 38%. This contrast is the main driver of the propagated uncertainty σ_prop reported for AGW in Table 4.

(2) Explaining into more details the NO_AGGREG sensitivity simulation: we investigate the dedicated test in which the number of source categories transported in the atmospheric model was increased from 5 to 14 (full sub-sector resolution), to evaluate the trade-off between computational efficiency and isotopic detail. The resulting differences in modeled atmospheric $\delta^{13}C–CH_4$ are small at global scale (+0.06‰ mean), with localized differences of up to ±0.5‰ in regions where sub-sector composition contrasts strongly with the global average (notably South Asia and the Middle East; see new Figure S4). This indicates that the limiting factor for AGW-related uncertainty is not the number of categories but rather the signature values of the existing sub-sectors and inventory-level flux partitioning between livestock and waste.

(3) Indo-Gangetic Plain regional case study (Section 4.3.1): we now show that AGW source signatures contribute up to 80% of local $\delta^{13}C–CH_4$ variance over this region, driven by the strong contrast between livestock and waste sub-sectors, with the relative livestock share varying from 67% (EDGARv8) to 79% (CEDS, GAINS) across inventories.

Manuscript change (Section 4.2.1, L 719–733): *" AGW is disaggregated in our framework into five sub-sectors (livestock, rice, landfills, wastewater, and agricultural waste; Table 1), each with its own isotopic signature and flux distribution. Livestock and rice together account for ~62% of AGW emissions and carry the most depleted signatures (−65.8 ‰ and −59.9 ‰), while waste-related sub-sectors (−50.9 to −56.2 ‰) make up the remaining 38%. This contrast is the main driver of the propagated uncertainty σprop reported for AGW in Table 4. To assess whether finer sectoral granularity, i.e. the number of source categories effectively resolved in the atmospheric model, would meaningfully change the modeled atmospheric signal, the NO_AGGREG simulation increases the number of source categories from 5 to 14 (Table 3). This is conceptually distinct from the aggregation uncertainty σagg defined in Sect. 2.3.3, which quantifies the sensitivity of the aggregated signature to the choice of flux inventory used for weighting. The resulting differences are small: +0.061 ‰ globally for δ13C-CH4 (Fig. S4). Localized differences of up to ±0.5 ‰ in δ13C-CH4 occur in regions where sub-sector composition contrasts strongly with the global average, notably in South Asia and the Middle East. These results indicate that increasing sectoral granularity beyond five sub-sectors does not substantially alter the modeled atmospheric isotopic signal at the global scale. Reducing AGW-related uncertainty would therefore benefit more from better-constraining the signature values of the existing sub-sectors and from refining inventory-level flux partitioning between livestock and waste, particularly in rapidly developing regions, than from increasing the number of source categories."*

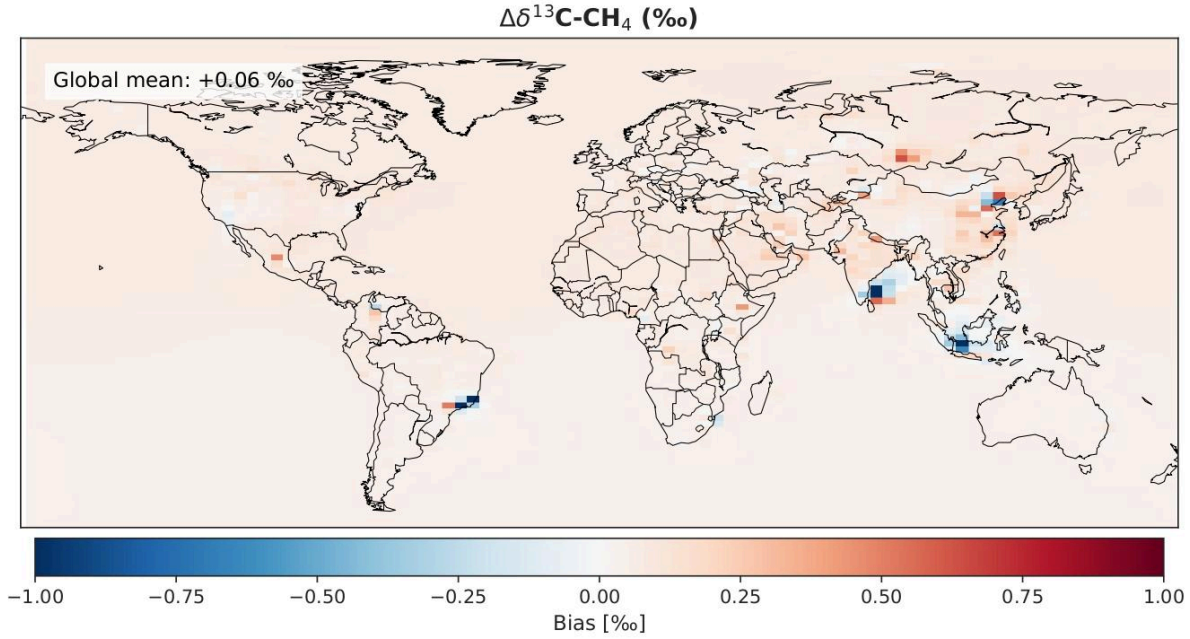

Figure S4. Difference maps between the NO_AGGREG (14 categories) and the reference OH_INCA simulation (5 categories) averaged over 2016–2020 at the surface level for $\Delta\delta_{13}$C-CH$_4$ (‰).

M4. Treatment of the OH kinetic isotope effect

Reviewer comment: "The results highlight OH-KIE as a dominant driver of δ^{13}C-CH$_4$ uncertainty, yet the treatment of this process is relatively simplified. Please expand the discussion of OH-KIE

parameterization, including laboratory constraints, variability, and implications for inversion systems."

Response: We agree this is an important point given the dominant role of OH-KIE. We have substantially expanded the discussion in Section 4.2.3 to cover:

(1) Laboratory constraints: the OH-KIE estimate relies on only two published experimental determinations (Cantrell et al. (1990): 1.0054 ± 0.0009 at 296 K; Saueressig et al. (2001): 1.0039 ± 0.0004 at 296 K). No measurements exist below 278 K, although theoretical calculations suggest the KIE may increase at lower temperatures (Gupta et al., 1997).

(2) Atmospheric leverage: at steady state, Fujita et al. (2020) showed that the 0.0015 difference between the two values yields a ~1.3‰ shift in atmospheric $\delta^{13}C\text{-}CH_4$. This high leverage explains why our sensitivity analysis ranks OH-KIE as the dominant chemistry-related driver of $\delta^{13}C–CH_4$ variability (RSD 2.2%, SD 0.40‰; Table 6).

(3) Practical implications for inversions: previous $\delta^{13}C\text{-}CH_4$ inversions have adopted either value (Saueressig et al. (2001) in Nisbet et al. (2016); Schaefer et al. (2016); Basu et al. (2022); Thanwerdas et al. (2024); Cantrell et al. (1990) in Rice et al. (2016)). This choice is absorbed by the posterior source mixture and represents an intrinsic uncertainty that cannot be reduced through prior refinement.

(4) Recommendation: we now recommend treating the full Cantrell–Saueressig range in inversion frameworks (see Section 4.3.2), either through ensemble-based approaches or explicit optimization within variational frameworks, until laboratory or theoretical advances narrow this range.

Manuscript change (Section 4.2.3, L 846–854): *"Regarding the kinetic isotope effect, Figure 6f and Figure S5f show that uncertainties in the OH-KIE induce a geographically homogeneous SD of 0.4‰ (RSD of 2.2%) in the atmospheric $\delta^{13}C\text{-}CH_4$ signal, exceeding the observed SD at surface stations. This sensitivity is driven by only two published experimental determinations of the $^{12}C/^{13}C$ KIE for CH_4 + OH: Cantrell et al. (1990) (1.0054 ± 0.0009 at 296 K) and Saueressig et al. (2001) (1.0039 ± 0.0004 at 296 K). No measurements exist below 278 K, although theoretical calculations suggest the KIE may increase at lower temperatures (Gupta et al., 1997). At steady state, Fujita et al. (2020) showed that the 0.0015 difference between the two values yields a ~1.3‰ shift in atmospheric $\delta^{13}C\text{-}CH_4$, illustrating the high leverage of this parameter. In practice, previous inversions have adopted either value, Saueressig et al. (2001) in e.g. Nisbet et al. (2016); Schaefer et al. (2016); Basu et al. (2022); Thanwerdas et al. (2024), and Cantrell et al. (1990) in e.g. Rice et al. (2016). This choice is absorbed by the posterior source mixture. Accordingly, we recommend treating the full Cantrell–Saueressig range in inversion frameworks (see Sect. 4.3.2)"*

M5. Other sinks: Cl oxidation and soil uptake

Reviewer comment: "The manuscript primarily focuses on OH oxidation, while other sinks (e.g., Cl oxidation, soil uptake) receive limited attention. Provide a more quantitative discussion of these additional sinks and their potential isotopic impacts."

Response: We agree this deserves a quantitative treatment. We have added a dedicated paragraph in Section 4.2.3 covering both sinks:

Chlorine sink: We now explicitly discuss its magnitude (~1–3% of total CH_4 oxidation; Hossaini et al., 2016; Sherwen et al., 2016; Gromov et al., 2018; Wang et al., 2021), the climatological tropospheric Cl sink of 6 [1–13] Tg CH_4 yr^{-1} reported by the latest Global Methane Budget (Saunois et al., 2025), and its exceptionally large KIE (≈1.066 at 298 K; Saueressig et al., 1995) which is more than an order of magnitude larger than that of OH. We provide a quantitative reference to Thanwerdas et al. (2022b), who quantified within the same CIF–LMDz–SACS framework as ours that mean tropospheric Cl perturbations of 1000 molec. cm^{-3} induce a near-linear sensitivity of +11.7 Tg CH_4 yr^{-1} and −1.0‰ in the globally averaged source signature, with stratospheric Cl alone contributing a ~0.30‰ surface enrichment in $\delta^{13}C$-CH_4 via stratosphere–troposphere exchange. We explain that we did not repeat a Cl sensitivity experiment because it would essentially duplicate this recent and comprehensive analysis with the same model, but we acknowledge the Cl sink as a leading factor limiting isotope-based source partitioning, in agreement with Basu et al. (2022) and Röckmann et al. (2024b).

Soil sink: We now explicitly discuss its magnitude (~31 [17–39] Tg CH_4 yr^{-1}, Saunois et al., 2025, or about 5% of the total CH_4 sink), its moderate KIE (≈1.020; Snover and Quay, 2000), intermediate between OH (1.0039) and Cl (1.066), and its dynamic implementation in our framework (first-order deposition process with isotope-dependent deposition velocities; Section 3.1.5). We argue that, given its small relative contribution, its moderate KIE, and its well-constrained global magnitude, soil uptake uncertainties are expected to have a substantially smaller impact on the modeled $\delta^{13}C$-CH_4 signal than OH-KIE, and were therefore not perturbed in the Monte Carlo ensemble.

We also added a footnote to Table 6 explicitly noting that the Cl sink is not perturbed independently in our sensitivity ensemble, with reference to Thanwerdas et al. (2022b).

Manuscript change (Section 4.2.3, new paragraph L 855–879): *“*

Beyond OH, two additional sinks contribute to the δ13C-CH4 budget and deserve explicit discussion: oxidation by chlorine (Cl) and soil uptake. Both are included in our forward simulations (Sect. 3.2) but were not perturbed in dedicated sensitivity experiments.

The Cl sink accounts for a small fraction of total CH4 oxidation. Recent estimates converge on a tropospheric contribution of ~1–3% of the total chemical sink (Hossaini et al., 2016; Sherwen et al., 2016; Gromov et al., 2018; Wang et al., 2021), with the latest Global Methane Budget reporting a climatological tropospheric Cl sink of 6 [1–13] Tg CH4 yr−1 (Saunois et al., 2025), substantially smaller and better constrained than earlier estimates (Allan et al., 2007). Despite this small magnitude, the Cl reaction carries an exceptionally large kinetic isotope effect (KIE ≈ 1.066 at 298 K; Saueressig et al., 1995), more than an order of magnitude larger than that of OH, so even modest uncertainties in Cl concentrations translate into substantial shifts in modeled δ13C-CH4 (see Table 2). Basu et al. (2022) further identified the combined uncertainty in fractionation (OH-KIE and Cl contribution) as the single most important factor limiting isotope-based source partitioning at the global scale (Röckmann et al., 2024b). Thanwerdas et al. (2022b) quantified this influence within the same CIF-LMDz-SACS framework used here, and reported a near-linear sensitivity of +11.7 Tg CH4 yr−1 and −1.0 ‰ in the

globally averaged source signature per 1000 molec. cm−3 increase in mean tropospheric Cl, with stratospheric Cl alone contributing a ~ 0.30 ‰ surface enrichment via stratosphere–troposphere exchange and modifying the δ13C-CH4 seasonal cycle amplitude by up to 10–20% depending on latitude. Because our configuration adopts the Cl field from Wang et al. (2021), consistent with the most recent tropospheric chlorine chemistry, the Cl-related uncertainty in our simulations is bounded by the ranges quantified in Thanwerdas et al. (2022b), which are of the same order of magnitude as the OH-KIE sensitivity reported in Table 6. A dedicated Cl sensitivity experiment was therefore not repeated here to avoid duplicating a recent and comprehensive analysis with the same model.

Soil uptake contributes ~ 31 [17–39] Tg CH4 yr−1 to the global CH4 budget (Saunois et al., 2025), or about 5% of the total CH4 sink, with a moderate KIE of ~ 1.020 (Snover and Quay, 2000), intermediate between OH (1.0039) and Cl (1.066) (see Table 2). In our framework, it is implemented as a first-order deposition process with isotope-dependent deposition velocities (Sect. 3.1.5). Given its small relative contribution to the total sink, its moderate KIE, and the well-constrained global magnitude reported in recent budgets, soil uptake uncertainties are expected to have a substantially smaller impact on the modeled δ13C-CH4 signal than the OH-KIE (Table 6), and were therefore not perturbed in the Monte Carlo ensemble."

M6. Schematic of the uncertainty propagation methodology

Reviewer comment: "The uncertainty propagation methodology is rigorous but complex and may be difficult for readers to follow. Maybe include a schematic diagram summarizing uncertainty components and clarify how these uncertainties are incorporated into inversion prior error structures."

Response: We agree, this is a very useful suggestion. We have added a new Figure 1 to Section 2.3, which provides a schematic overview of the full uncertainty propagation pathway:

• Sub-sector isotopic uncertainties σ_i, derived from Monte Carlo simulations (lower bound) and literature standard deviations (upper bound);

• Propagation to the sector level (σ_prop) via flux-weighted error propagation (Eq. 3);

• Aggregation uncertainty (σ_agg), estimated from sensitivity tests using different emission inventories (Eq. 5);

• Combination into total sectoral uncertainty (σ_total, Eq. 2; Table 4);

• Use of σ_total in inversion frameworks: either to inform the prior error covariance matrix B (if isotopic source signatures are optimised), or the observation error covariance matrix R (if they are held fixed).

We also added an introductory paragraph in Section 2.3 referencing this new schematic and laying out the overall structure of the propagation chain. Combined with the Figure 4 (showing how uncertainties propagate through the inversion) and the Figure 10 (clarifying the effect of including $\delta^{13}C–CH_4$ constraints in the inversion), readers now have a complete visual narrative from sub-sector measurements to inversion error structures.

Manuscript change (Section 2.3, new introductory paragraph L 190–194): *"This section describes how uncertainties in aggregated $\delta^{13}C\text{-}CH_4$ source signatures are estimated. (...) The overall propagation pathway, from sub-sector measurements to inversion error structures, is summarized schematically in Fig. 1. In what follows, we describe the three components of this propagation chain: the total uncertainty σ_total combining all contributions (Sect. 2.3.1), the propagated uncertainty σ_prop derived from sub-sector variability (Sect. 2.3.2), and the aggregation uncertainty σ_agg reflecting inventory choices (Sect. 2.3.3)."*

New Figure 1: *Schematic overview of the uncertainty propagation pathway for $\delta^{13}C\text{-}CH_4$ source signatures, linking sub-sector uncertainties (σ_i) through flux-weighted propagation (σ_prop) and inventory-based aggregation tests (σ_agg) to the total sectoral uncertainty (σ_total), and then to the B and R matrices in atmospheric inversion frameworks.*

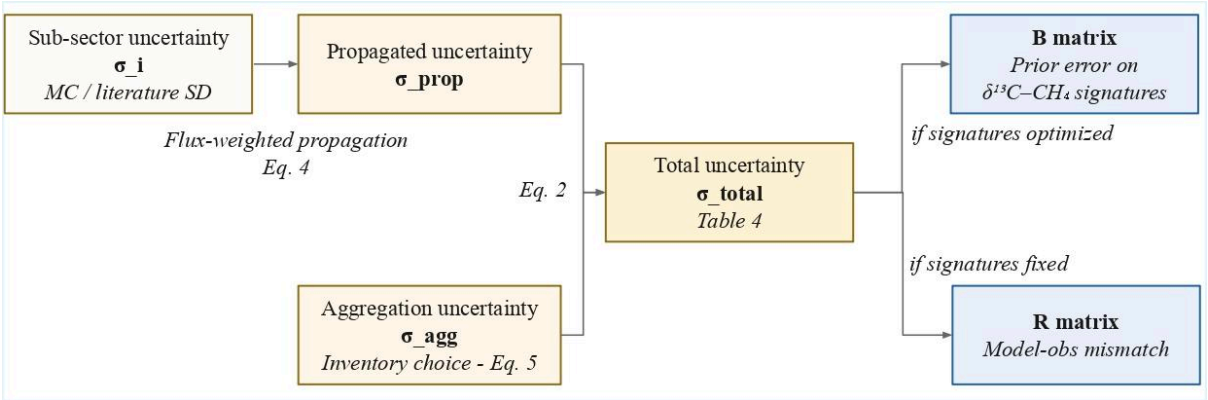

Fig.1 Schematic overview of the uncertainty propagation pathway for $\delta^{13}C\text{-}CH_4$ source signatures. Sub-sector isotopic uncertainties(σ_i), derived from Monte Carlo simulations (lower bound) and literature standard deviations (upper bound), are propagated to the sectorlevel (σ_{prop}) via flux-weighted error propagation (Eq. 3). The aggregation uncertainty (σ_{agg}), estimated from sensitivity tests using dif-ferent emission inventories (Eq. 5), is combined with$\sigma_{prop}$to yield the total sectoral uncertainty (σ_{total}, Eq. 2). In atmospheric inversionframeworks,σ_{total}informs either the prior error covariance matrix (B) if isotopic source signatures are optimized, or the observation error covariance matrix (R) if they are held fixed (see Sect. 4.3.2)

M7. Single transport model (LMDz)

Reviewer comment: "All simulations are conducted using a single atmospheric transport model (LMDz), without discussion of model-related uncertainties. Discuss the potential influence of transport model choice and resolution on the results."

Response: We acknowledge this limitation, which is intrinsic to a single-model study. We have added a dedicated discussion in Section 4.4 (Pathways for improvement) addressing transport-related uncertainty in three respects:

(1) Model spread for CH_4 budgets: the TransCom-CH_4 intercomparison (Patra et al., 2011) showed that modeled CH_4 budgets are sensitive to troposphere–stratosphere exchange rates and to vertical grid structure, with CH_4 lifetimes spanning 9.50–10.27 yr across 12 CTMs using identical OH fields.

(2) Specific implications for $\delta^{13}C$–CH_4: vertical transport additionally controls the rate at which ^{13}C-enriched stratospheric air re-enters the troposphere via the Brewer–Dobson circulation, as well as the vertical distribution of the Cl sink and its strong fractionation (Butchart, 2014; Thanwerdas et al., 2022b).

(3) Robustness argument: the sensitivity hierarchy identified in our study (dominated by OH-KIE and AGW signatures) is driven by prescribed inputs (oxidant fields, source signatures) rather than by transport, and is therefore expected to be robust across CTMs. Quantifying transport-related uncertainty through multi-model ensembles, by extending the TransCom-CH_4 framework to include both CH_4 and $\delta^{13}C$-CH_4, remains a priority for future work and complements the dataset distributed here, which can be used by other inversion systems with their own transport models.

We also explicitly acknowledge the LMDz horizontal resolution (3.75° × 1.875°) in Section 3.1.1 and now state in Section 4.4 that "all simulations were performed with LMDz at a single resolution" as a caveat.

Manuscript change (Section 4.4, transport paragraph L 1029–1038): *"A second priority concerns atmospheric transport and chemistry, which were not perturbed in our sensitivity ensemble. All simulations were performed with LMDz at a single resolution (Sect. 3.1.1), and the TransCom-CH_4 intercomparison (Patra et al., 2011) showed that modeled CH_4 budgets are sensitive to troposphere–stratosphere exchange rates and to vertical grid structure, with CH_4 lifetimes spanning 9.50–10.27 yr across 12 CTMs using identical OH fields. For $\delta^{13}C$-CH_4, vertical transport additionally controls the rate at which ^{13}C-enriched stratospheric air re-enters the troposphere via the Brewer–Dobson circulation. The sensitivity hierarchy identified here, dominated by OH-KIE and AGW signatures, is driven by prescribed inputs and is expected to be robust across CTMs, but quantifying transport-related uncertainty through multi-model ensembles remains a priority."*

M8. Detailed regional analyses

Reviewer comment: "The manuscript identifies regions with high isotopic uncertainty but does not explore them in depth. Include more detailed regional analyses or case studies, particularly for key methane-emitting regions."

Response: We agree this is essential, especially because Figure 9 (now extensively discussed) reveals that the dominant uncertainty drivers are strongly heterogeneous across the globe. We have added three explicit regional case studies in Section 4.3.1:

(1) Indo-Gangetic Plain: AGW source signatures contribute up to 80% of the local $\delta^{13}C$–CH_4 variance over this region. We quantify both the magnitude (~26 Tg CH_4 yr^{-1} from EDGARv8 over 2016–2020) and the source of the spread (relative livestock share varies from 67% in EDGARv8 to 79% in CEDS/GAINS, generating direct propagation to atmospheric $\delta^{13}C$–CH_4). The Ethiopian highlands

provide a finer-scale illustration of the C_3/C_4 forage balance varying with altitude (Brychkova et al., 2022). We also reference emerging dual-isotope evidence over South Asia (Yao et al., 2026).

(2) Tropical wetlands (Congo Basin, Amazon, Borneo): wetland flux uncertainties dominate, reaching more than 60% of local variance in Borneo. We note that recent tropical airborne and ground-based campaigns (France et al., 2022; Nisbet et al., 2021; Shaw et al., 2022) have begun addressing the data gap but cover only a limited number of sites.

(3) Caspian region: freshwater flux uncertainties account for more than 60% of local $\delta^{13}C–CH_4$ variance, due to the classification ambiguity of this brackish endorheic lake combined with proximity to major oil and gas infrastructure in Turkmenistan and Azerbaijan.

These regional analyses are then linked to a key conceptual distinction in Section 4.3.2 between two regimes of uncertainty: localized hotspots, where targeted external efforts (inventories, field campaigns, process models) can reduce prior errors, and remote/well-mixed background regions, where uncertainties are dominated by OH-KIE and require explicit optimization within the inversion framework.

Manuscript change (Section 4.3.1, new regional case studies subsection L 942–965): *"Four regional case studies illustrate the diversity of dominant drivers and provide context for the targeted improvements discussed in Sect. 4.3.2 and Sect. 4.4. – Indo-Gangetic Plain: AGW source signatures contribute up to 80% of the local $\delta^{13}C$-CH_4 variance (...). – Tropical wetlands (Congo Basin, Amazon, Borneo): Wetland flux uncertainties dominate over these regions, reaching more than 60% of local $\delta^{13}C$-CH_4 variance in Borneo (...). – Caspian region: Freshwater flux uncertainties account for more than 60% of the local $\delta^{13}C$-CH_4 variance (...)."*

M9. Satellite observations – quantitative limitations

Reviewer comment: "The manuscript includes a forward-looking discussion on satellite observations (e.g., GOSAT, TROPOMI), but this remains largely conceptual. Clarify current technical limitations and, if possible, provide quantitative estimates of detection capabilities."

Response: We agree, the satellite discussion was too conceptual. We have substantially revised the corresponding paragraph in the Conclusions to provide quantitative estimates of detection capabilities, and we now address two distinct issues:

(1) Precision gap: Malina et al. (2019) report individual $^{13}CH_4$ retrieval uncertainties of <1 ppb for TROPOMI and <0.68 ppb (<0.2 ppb in high-SNR cases) for Sentinel-5/UVNS, whereas the target $\delta^{13}C$ uncertainty of <1‰ required to differentiate source types corresponds to a $^{13}CH_4$ uncertainty of <0.02 ppb, a gap of one to two orders of magnitude that requires significant spatial and/or temporal averaging.

(2) Systematic errors: $^{13}CH_4$ retrievals are highly sensitive to errors in a priori temperature and pressure profiles (Malina et al., 2019).

A dedicated detectability assessment is planned as a follow-up to the present work, building on the isotopic maps and sensitivity framework developed here, and aiming to quantify the spatial and temporal scales at which GOSAT, TROPOMI and IASI could detect $\delta^{13}C\text{-}CH_4$ signals above their respective noise floors. We mention it to indicate the trajectory of follow-up work that the present dataset is designed to support.

Manuscript change (Conclusions, satellite paragraph L 1086–1095): *"Finally, the increasing availability of satellite-based CH_4 and isotopic measurements opens promising perspectives for constraining methane sources at the global scale. (...) Individual $^{13}CH_4$ retrieval uncertainties remain large: Malina et al. (2019) report mean uncertainties of <1 ppb for TROPOMI (SWIR3 channel) and <0.68 ppb for Sentinel-5/UVNS (SWIR1 channel), whereas the target $\delta^{13}C$ uncertainty of <1‰ required to differentiate between source types corresponds to a $^{13}CH_4$ uncertainty of <0.02 ppb. Significant spatial and/or temporal averaging is therefore required to reduce uncertainties to detectable levels. In addition, $^{13}CH_4$ retrievals are highly sensitive to errors in a priori temperature and pressure profiles, which can introduce systematic biases (Malina et al., 2019). A dedicated detectability assessment will be essential to evaluate whether current or forthcoming missions can effectively detect and interpret atmospheric isotopic variations under real conditions."*

M10. Readability of uncertainty propagation and sensitivity analysis sections

Reviewer comment: "While the manuscript is generally well organized, some sections, particularly those describing uncertainty propagation and sensitivity analyses, are dense and difficult to follow. Please improve readability by summarizing key findings at the end of sections and reducing redundancy between the Results and Discussion."

Response: We agree, this is a fair criticism, and we have implemented several structural improvements:

(1) End-of-section summaries: we added concise summary paragraphs at the end of each main results sub-section (4.1.1, 4.1.2, 4.1.3, 4.2.1, 4.2.2, 4.2.3, 4.2.4) highlighting the key findings in 2–3 sentences. For example, Section 4.2.1 now ends with: "In summary, two distinct aggregation-related effects have been tested in this section. (...) Both aggregation-related choices therefore have a limited impact on atmospheric simulations, supporting the transferability of the updated maps across inversion systems and inventories."

(2) Restructured Discussion: Section 4.3 has been reorganised into three clearly-distinguished sub-sections: 4.3.1 Key uncertainty drivers (synthesis of sensitivity results, no redundancy with Section 4.2); 4.3.2 Implications for isotopic inversions (recommendations only, with practical bullet points); 4.3.3 Pathways for improvement (renumbered and restructured into three thematic axes: temporal representativeness, transport and chemistry, process-level understanding).

(3) Reduced redundancy: we systematically removed text overlapping between Sections 4.2 and 4.3. Section 4.3.1 now references Section 4.2 results without re-explaining them, focusing instead on integration and ranking.

We hope these revisions substantially improve readability while preserving the rigour of the methodology.

Closing remarks

We thank Reviewer 2 once again for the constructive critique. We believe the revisions outlined above, including the new model–observation comparison (Section S4 of the Supplement), the explicit treatment of inter-dataset systematic biases, the additional NO_AGGREG sensitivity simulation, the expanded chemistry discussion (OH-KIE, Cl, soil uptake), the new schematic figure (Fig. 1), the regional case studies, the quantitative satellite assessment, and the structural improvements in readability, address all ten major comments. We are confident the revised manuscript is substantially strengthened and we hope it now meets the expectations of the reviewer and the editor.

Summary of new material added in response to Reviewer 2

- New Figure 1 (Section 2.3): schematic overview of the uncertainty propagation pathway from sub-sectors to inversion B/R matrices.
- Substantial revision to NO_AGGREG sensitivity simulation (Section 4.2.1): tests increasing the number of source categories from 5 to 14 (Figure S4).
- New Section 4.3.1 regional case studies: Indo-Gangetic Plain, tropical wetlands (Congo Basin, Amazon, Borneo), Caspian region.
- New Section S4 in the Supplement: model–observation comparison including globally averaged time series (Figure S11) and inter-hemispheric gradient diagnostics (Figure S12).
- Substantial revisions to Section 4.1.4 (Comparison with previous datasets): three categories of systematic biases explicitly identified and discussed.
- Substantial revisions to Section 4.2.3 (Atmospheric chemistry): expanded OH-KIE discussion with laboratory constraints, Fujita et al. (2020) leverage analysis, and inversion implications; new dedicated paragraph on Cl and soil sinks.
- Restructured Section 4.3 (Discussion): split into 4.3.1 Key drivers, 4.3.2 Inversion implications, 4.3.3 Pathways for improvement.
- End-of-section summaries added throughout Sections 4.1 and 4.2.
- Quantitative satellite detectability discussion in the Conclusions.